Development of a melt pool characteristics detection platform based on multi-information fusion of temperature fields and photodiode signals in plasma arc welding

Zhuangzhuang Mao[1] · Wei Feng[1] · Xiao Han[2] · Heng Ma[3] · Ce Hao[4] · Changmeng Liu[2] · Zhanwei Liu[1]

Abstract

Melt pool characteristics reflect the formation mechanisms and potential issues of flaws. Long-term, high-precision, and real-time detection of melt pool characteristics is one of the major challenges in the industrial application of additive manufacturing technology. This work proposes, for the first time, the melt pool characteristics detection platform based on multi-information fusion in the plasma arc welding (PAW) process, which fully utilizes real-time photodiode signals and high-precision, information-rich melt pool temperature fields. By optimizing the detection area and wavelength selection of the platform, particularly through the unique photodiode signal acquisition system capable of detecting the high-sensitivity area of the melt pool, we effectively mitigate the influences of intense arc light and welding wire obstruction on the temperature signals and photodiode signals. Through applying machine learning, the trained model integrates photodiode signals with temperature signals from the high-sensitivity area, thereby achieving real-time acquisition of high-precision average temperature. By combining the fused signals collected from the platform and the scanning results from micro-computed tomography (CT), we evaluate and verify the influence of flaws and droplets on the melt pool characteristics, realizing the determination of flaw occurrence based on the abnormal variations of average temperature. The experimental results demonstrated that the platform fully utilized the advantages of long-term and real-time acquisition of the photodiode signal and the high-precision and information-rich of the melt pool temperature field, achieving long-term, high-precision, and real-time detection of melt pool characteristics.

✉ Changmeng Liu
liuchangmeng@bit.edu.cn

✉ Zhanwei Liu
liuzw@bit.edu.cn

[1] School of Aerospace Engineering, Beijing Institute of Technology, Beijing 100081, China

[2] School of Mechanical Engineering, Beijing Institute of Technology, Beijing 100081, China

[3] AVIC Xi'an Aircraft Industry (Group) Co., Ltd., Xi'an 710089, Shaanxi, China

[4] AECC Commercial Aircraft Engine Co. Ltd., Shanghai 200241, China

Introduction

Metal additive manufacturing (AM) technology usually incorporates powder bed fusion (PBF) or directed energy deposition (DED) (Everton et al., 2016). Depending on the heat sources, PBF mainly occurs through selective laser melting (SLM) and electron beam melting (EBM), while DED mainly occurs through laser engineered net shaping (LENS) and wire arc additive manufacturing (WAAM) (Xia et al., 2022). As one type of WAAM, plasma arc welding (PAW) is a fusion welding method using a plasma arc high-energy density beam as the welding heat source. PAW has advantages such as energy concentration, high productivity, fast welding speed, low stress and deformation, and a stable arc. Compared with traditional subtractive manufacturing, a WAAM

system can reduce manufacturing time by 40–60% and post-processing time by 15–20% depending on part sizes (Wu et al., 2018). Because PAW uses an arc as the heating source, it has different characteristics from other high-energy beams such as lasers: the area of the metal melt pool is relatively large, the change in the melt pool is intense during the forming process, the melt pool is more affected by the stability of the arc welding power source, and the change in the surrounding environment maintains the melt pool in an unstable state. Therefore, the most advanced PAW may still produce flaws and other anomalies even under the optimal printing parameters, which is the key factor limiting the further development of this technology.

As the basic macro-level unit of a production sample, the melt pool characteristics can embody whether the sample is abnormal. Many in situ monitoring studies of melt pools in metal AM processes (Wang & Kovacevic, 2002; Wang & Chen, 2002; Zhang et al., 2014; Liu et al., 2017a, 2017b, 2017c, 2017d; Wu et al., 2021) have been conducted. In our previous work, we monitored melt pools under SLM (Ma et al., 2022; Mao et al., 2023) and LENS (Feng et al., 2022; Hao et al., 2020) processes. In addition, the monitoring of melt pools under EBM (Boone et al., 2018) and WAAM (Liu et al., 2013; Saad et al., 2006; Veiga et al., 2022; Zhang et al., 2022) has also been studied by many researchers. Sensors were used for data acquisition in all these studies (Liu et al., 2017a, 2017b, 2017c, 2017d; Wu et al., 2020), so it is important to select appropriate sensors for the in situ monitoring of melt pool characteristics. During the monitoring process, photodiodes and cameras are sensors used for the acquisition of melt pool characteristic data.

Photodiodes are widely used in the industrial field of metal AM because of their fast response, low redundant data, online monitoring, and low price (Berumen et al., 2010; Clijsters et al., 2014; Gökhan et al., 2018; Kruth et al., 2007; Liu et al., 2017a, 2017b, 2017c, 2017d). Photodiodes are currently mainly used for characteristic detection of the melt pool in the SLM process. For example, Taherkhani et al. (2021) developed a flaw detection platform using photodiode signals emitted from the melt pool of SLM, and pores larger than 120 μm initiated from the lack of fusion phenomena could be detected. Photodiode signals were used to establish an association model with various SLM process parameters and key geometry features through a machine learning algorithm, and the effectiveness of the forward model and inverse model was demonstrated. Through a data-driven method, experimental diagnosis was used to optimize laser process parameters before printing (Lapointe et al., 2022). The feature data extracted from three different photodiodes in SLM were processed by several unsupervised clustering methods, and the goal of predicting the final construction quality measurement based on purely photodiode data was achieved (Jayasinghe et al., 2022). The photodiode data under SLM were correlated with the scanner position and the laser state during the buildup of Inconel-718 components under varying powers, scan speeds, and hatch spacing parameters through a line-to-continuum approach. Then, the photodiode data were compared against post-build computed tomography scans to prove that the photodiode data were related to the processing conditions and manufacturing quality (Dunbar et al., 2018). Mao et al. (2023) proposed a continuous online flaw detection method combining the photodiode signal and melt pool temperature based on deep learning algorithms in SLM, and a robust correlation could be established between the photodiode signal and the average melt pool temperature through the neural network. In addition, under the LENS process, a photodiode was also used to characterize the change in a melt pool, and a statistical method was used to handle photodiode signal data with variations in the laser power, scanning velocity, and powder feeding rate (Zhang et al., 2021). However, there are few studies on photodiodes used in the PAW process. Wang and Kovacevic (2002), Wang and Chen (2002) used a photodiode to obtain the light signal of the efflux plasma and provide a reference signal of the keyhole status instead of using the photodiode for the characteristic detection of the melt pool. Analogously, Saad et al. (2006) used a photodiode to monitor the keyhole mode from the backside of the sample without collecting the melt pool signals. However, from these literatures, it is evident that the application of photodiodes in AM is relatively rudimentary. Because the detection area of photodiodes is often uncertain or much larger than the melt pool area, many interfering light sources other than the radiated light from the melt pool can potentially affect the accuracy of the photodiode signal in representing melt pool characteristics. The theoretical significance of photodiode signals and how to more accurately represent melt pool characteristics using photodiode signals have not yet received attention from researchers.

Cameras have been utilized for melt pool monitoring because pixels give the signal spatial resolution, and the common cameras are CCD and CMOS (Spears et al., 2016). The signals captured by the camera have two main purposes: one is to directly measure the morphology of the melt pool (de Winton et al., 2021), and the other is to obtain the melt pool temperature field by combining the principle of dual-wavelength thermometry (Feng et al., 2022; Hao et al., 2020; Ma et al., 2022; Mao et al., 2023). This work focuses more on the application of the latter. The melt pool temperature field obtained from camera signals is primarily used in LENS and SLM processes, but its application in the PAW process is still not mature. Many studies have demonstrated the correlation between melt pool temperature and the macroscopic and microscopic structures of the samples (Hojjatzadeh et al., 2019; Kirka et al., 2020; Sun et al., 2020; Rezaeifar & Elbestawi, 2021). The rich information provided

by melt pool temperature can be utilized for flaw identification (Feng et al., 2022; Mao et al., 2023). For example, Ma et al. (2022) used the temperature field to obtain the characteristics of temperature distribution, profile, temperature gradient, and cooling rate of a melt pool. Mao et al. (2023) took the melt pool temperature field as the ground-truth to verify whether flaws are generated in the SLM process and confirmed the accuracy of the photodiode signal's prediction of flaws. Feng et al. (2022) utilized the similarity of the melt pool temperature field to conduct online flaw detection in the LENS process. Using the melt pool temperature field as the medium, Hao et al. (2020) verified the accuracy of an online measurement system developed under the LENS process. Khanzadeh et al. (2019) realized high-precision prediction of porosity location based on the temperature distribution of a melt pool during the LENS process. Kriczky et al. (2015) used coaxial thermal images collected during the LENS process to analyze and visualize thermal metrics, which enabled the assessment of part quality. However, the application of the melt pool temperature field in the PAW process is still not mature, mainly due to factors such as intense arc light and welding wire obstruction, which prevent the acquisition of a complete and accurate temperature field. In addition, existing high-speed cameras for collecting the melt pool temperature field are usually limited by transmission rate and memory storage capacity, resulting in their inability to work for a long time at high acquisition frame rates.

The latest research on real-time detection of AM (Ren et al., 2023) involves the use of machine learning to establish a training model for high-speed synchronized X-ray imaging and thermal imaging signals. This enables real-time detection of keyhole flaws based on thermal imaging signals. However, the high cost and limited penetration capability of high-speed synchronized X-ray imaging prevent its full application in practical industrial additive manufacturing processes.

Therefore, to address the challenges of high cost, small melt pool size, uncertain detection area of photodiode, low accuracy of photodiode signal, inability to obtain long-term melt pool temperature signals, and interference from intense arc light and welding wire obstruction in real-time detection of the PAW process, this work develops a multi-information fusion-based melt pool characteristics detection platform that fully utilizes real-time photodiode signals and high-precision and information-rich melt pool temperature fields. The platform mainly consists of a unique photodiode signal acquisition system and a designed temperature signal acquisition system, featuring three main innovative functionalities that directly contribute to the performance improvement of the melt pool characteristics detection platform.

Firstly, the high-sensitivity areas of the signals can be determined, especially the high-sensitivity area of the photodiode signals, which can be identified by the unique photodiode signal acquisition system. Our previous work (Feng et al., 2022) has demonstrated that the front heating region of the melt pool temperature field exhibits a more sensitive response to flaws, particularly to the response of open void flaws. The unique photodiode signal acquisition system enables the detection of the highly sensitive area of the melt pool. By optimizing and determining the detection area of the platform, we simultaneously obtain temperature signals and photodiode signals from the front heating region of the melt pool, while effectively avoiding the influence of intense arc light and welding wire obstruction.

Secondly, the average temperature of the melt pool can be obtained in real time. Through utilizing machine learning, we develop a method to represent the photodiode signals from the high-sensitivity area of the melt pool as the temperature signals, thereby achieving real-time acquisition of the average temperature of the melt pool with high precision.

Thirdly, the presence of flaws can be determined in real time through the analysis of the average temperature. The main oscillation frequency and the temperature field evolution process of the melt pool can be estimated separately using the photodiode signals and the temperature signals. By combining the grayscale image of the melt pool and the photodiode signals, the abnormal variations in melt pool characteristics caused by droplets are estimated. Similarly, by combining the rich information from the melt pool temperature field and the scanning results from micro-computed tomography (CT), the abnormal variations in melt pool characteristics caused by flaws also are estimated. Therefore, once the model is established, the presence of flaws can be determined by monitoring the real-time output of the average temperature.

The workflow of the melt pool characteristics detection platform based on multi-information fusion is shown in Fig. 1. The platform is mainly composed of a photodiode signal acquisition system and a temperature signal acquisition system. The photodiode signal acquisition system captures the photodiode signals, which are used to estimate the main oscillation frequency of the melt pool. Meanwhile, the temperature signal acquisition system captures the temperature signals, which are used to evaluate the evolution process of the melt pool temperature field. First, the signals from the high-sensitivity area of the melt pool, including the photodiode signals and temperature signals, are used to train a model through a machine learning approach. Then, this model converts the input photodiode signals into the average temperature of the melt pool. Finally, the presence of flaws can be determined by analyzing the abnormal variations in the average temperature signal output. Additionally, the melt pool temperature field and CT scanning results are used to verify the presence of flaws.
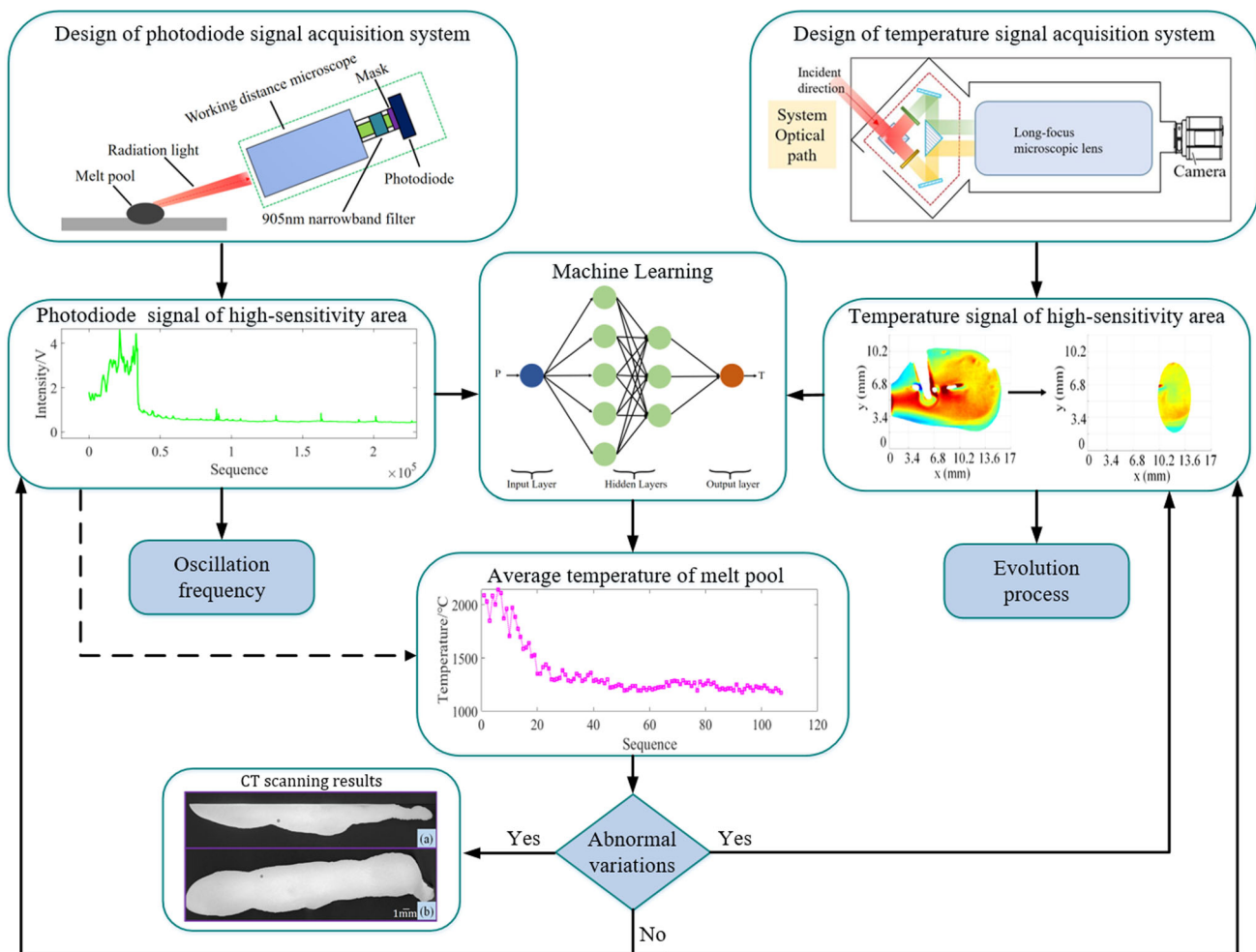
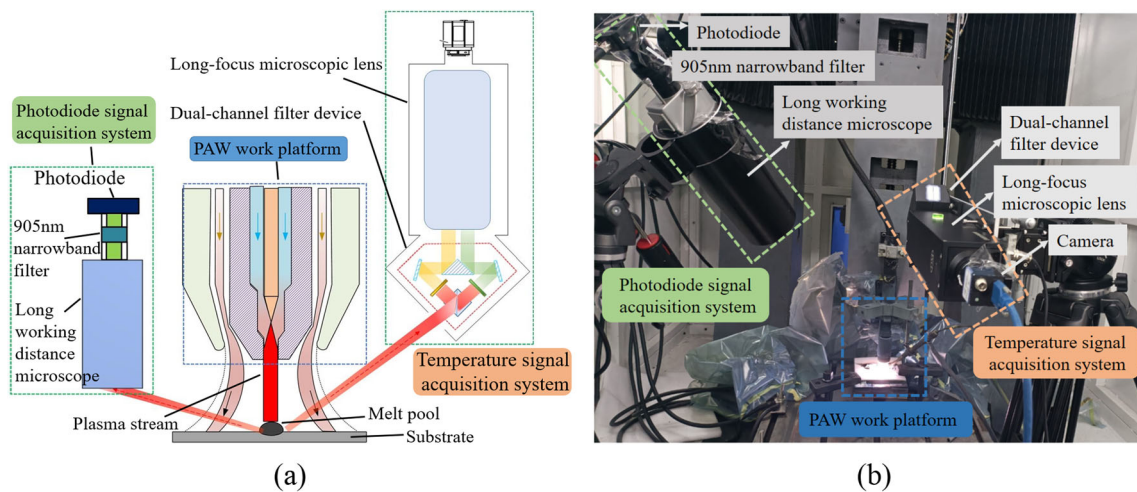**Fig. 1** Workflow of melt pool characteristics detection platform based on multi-information fusion

Fig. 2 Developed melt pool characteristic detection platform. **a** Schematic diagram. **b** Physical diagram

Platform design

Figure 2 a and b are schematic and physical diagrams of the developed melt pool characteristic detection platform, respectively. The platform primarily consists of the photodiode signal acquisition system and the temperature signal acquisition system. In "Design of photodiode signal acquisition system" and "Design of temperature signal acquisition system" sections, we will provide detailed explanations of the design rationale and composition of the photodiode signal acquisition system and the temperature signal acquisition system.

Theoretical analysis and verification of photodiode signals

The theoretical analysis and experimental verification of photodiode signals are helpful in providing support for the representation of melt pool characteristics. PDA100A2 is an amplified, switchable-gain silicon detector designed for the detection of light signals ranging from 320 to 1100 nm. The responsivity $R(\lambda)$ of the photodiode can be defined as the ratio of the photocurrent I_{PD} generated at a given wavelength to the incident light power P:

$$R(\lambda) = \frac{I_{PD}}{P} \tag{1}$$

Thus,

$$U = I_{PD}R_{\Omega} = R(\lambda)PR_{\Omega} \tag{2}$$

where R_{Ω} represents a constant resistance. Therefore, at a given wavelength, the output signal of the photodiode is the one-dimensional voltage value U, which is proportional to the incident light power P. The incident light power P is the energy passing through a certain Section S in unit time (note that it is a certain section, not a unit section), so the incident light power P is proportional to the area S.

The detection platform focuses on high precision, so it is necessary to verify whether the error of the output signal of photodiode PDA100A2 is within the acceptable range. The light of the adjustable power lamp is shot into the photodiode fixed on the wall, which is perpendicular to the flat wall. To confirm whether the light in the collection area of the photodiode is uniform, as shown in Fig. 3a, a camera is used to replace the photodiode to collect the gray information of the detection area. The average value, average difference value, and average relative difference value of the gray of the circular detection area collected by the camera are 220.10, 3.68, and 1.6%, respectively. To ensure that the incident light is at a constant wavelength, the camera is equipped with a 650 nm narrowband filter. The central wavelength of the narrowband

filter is not often a constant value. The central wavelength of the 650 nm narrowband filter is 650 ± 10 nm. Therefore, the error of the gray value is acceptable, and the light in the collection area of the photodiode is considered uniform and parallel.

To verify the relationship between the output signal of the photodiode and the detection area, as shown in Fig. 3b, rings with small radii r of 1 mm, 2 mm, and 3 mm are placed at the front of the photodiode to change the actual detection area of the photodiode. The specific steps of the experimental verification are as follows: 1. Place a ring with a small radius of 1 mm at the front end of the photodiode; 2. Fix the 650 nm narrowband filter on the front end of the photodiode; 3. Collect the photodiode signal at this time; 4. Turn on the lamp, set the light power to 70%, and use the data acquisition card to obtain the photodiode signal; 5. Set the light power to 90%, and use the data acquisition card to obtain the photodiode signal; 6. Turn off the lamp, place the rings with small radii of 2 mm and 3 mm at the front end of the photodiode, and repeat steps 2–5.

Tables 1 and 2 show the output photodiode signals before and after the lamp is turned on when the light power is set to 70% and 90%, respectively.

Therefore, the signal generated by the lamp is in direct proportion to the detection area (πr^2). The photodiode signal corresponding to the ring with a small radius of 1 mm is taken as the reference, and whether the photodiode signal is within a reasonable range is judged by analyzing the error of the theoretical and actual ratio of the ring with small radii of 2 mm and 3 mm to the reference. The error between the actual ratio of the photodiode signal and the reference of the ring with small radii of 2 mm and 3 mm and the theoretical ratio is within 10%, and the minimum error is only 0.5%. Since the distance between the lamp and the photodiode is 1.5 m, the 650 nm narrowband filter further filters the light intensity of the lamp into the photodiode, and the photodiode signal generated by the lamp is small. Due to the influence of factors such as the incomplete accuracy of the ring size, the incomplete flatness of the ring itself, and the weak effective light intensity, the error between the actual ratio and the theoretical ratio of the photodiode signal is acceptable.

Design of photodiode signal acquisition system

As shown in Fig. 2, the photodiode signal acquisition system mainly consists of a photodiode, a data acquisition card, a 905 nm narrowband filter, and a long working distance microscope. The details of the photodiode are introduced in "Theoretical analysis and verification of photodiode signals" section. The long working distance microscope has excellent linearity, depth of field, small distortion, and chromatic aberration. In addition, the working distance is 0.55–1.7 m, the field of view range is 0.9–15 mm, the resolution is 2.7 μm,

Fig. 3 Schematic diagram. **a** Experimental verification of light uniformity. **b** Experimental verification of relationship between photodiode signal and detection area

(a)   (b)
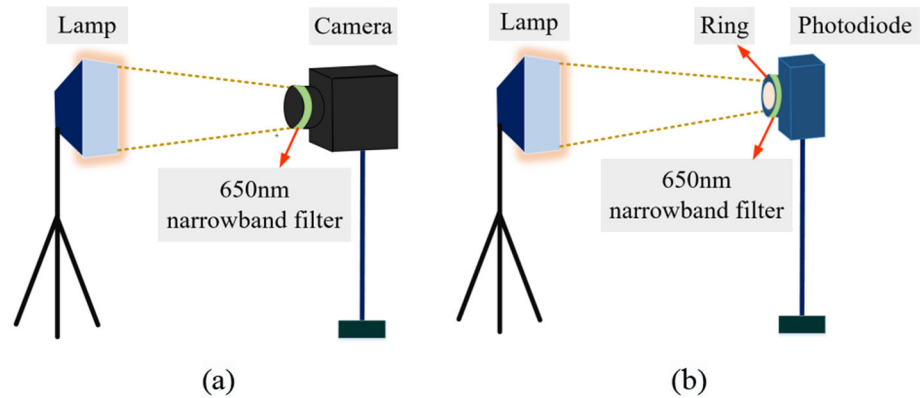
Table 1 Photodiode signals before and after the lamp is turned on when the light power is 70%

Output signals / V — Ring with small radius r	1 mm	2 mm	3 mm
Signal before lamp turned on	0.013944	0.013936	0.013958
Signal after lamp turned on	0.01419	0.014829	0.015883
Signal generated by lamp	0.000246	0.000893	0.001925
Theoretical ratio		4	9
Actual ratio		3.63	7.83

Table 2 Photodiode signals before and after the lamp is turned on when the light power is 90%

Output signals/ V — Ring with small radius r	1 mm	2 mm	3 mm
Signal before lamp turned on	0.014074	0.014073	0.014063
Signal after lamp turned on	0.01432	0.015112	0.016291
Signal generated by lamp	0.000246	0.001039	0.002228
Theoretical ratio		4	9
Actual ratio		4.22	9.05

and the selected 16 mm eyepiece can achieve $125\times$ magnification.

In the Introduction, we have analyzed that the current research work suffers from the uncertain detection area of the photodiode, which results in difficulty in accurately representing the melt pool characteristics using the collected photodiode signals. Therefore, the design of a photodiode signal acquisition system with a defined detection area is necessary. This work creatively designs a photodiode signal acquisition system that can determine the detection area. The camera in the system is used to determine the detection area,

and then the camera is replaced with the photodiode. Therefore, the detection areas of the photodiode and the camera will only be the same when their image distances are equal. Therefore, only when the image distances of the photodiode and the camera are equal, the detection area of the two sensors can be identical. As shown in Fig. 4, the distance between the upper surface of the camera and its target surface is 3.4 mm, and the distance between the upper surface of the photodiode and its target surface is 3.3 mm. According to the length of the connecting sleeve between the photodiode and camera with the long working distance microscope in Fig. 4, when 17.4 mm + 30 mm + X = 3.3 mm + 13.5 mm + 26.2 mm + 7.4 mm, the unity of the photodiode and camera in image distance can be achieved. Therefore, X = 3 mm is required and can be achieved by adjusting the thread.

After achieving the physical alignment of the image distances, experimental verification is conducted to determine whether the detection area error between the photodiode and the camera is within an acceptable range. The specific steps of the experimental verification are as follows: 1. As shown in Fig. 5, place the iron plate with a hole of 3 mm in diameter in front of the lamp; 2. Connect the camera with a ring with a small radius of 3 mm and a 650 nm narrowband filter to the long working distance microscope through the connecting sleeve; 3. Adjust the camera position to focus, and make the field of the camera almost identical to that of the hole; 4. Set the light power to 40%, 60%, 80%, and 100%, and collect the gray image. 5. Replace the camera and its connecting sleeve with the photodiode and its connecting sleeve, set the light power to 40%, 60%, 80%, and 100%, and collect the signal.

Equation (2) illustrates that the photodiode signal represents the integration of the light intensity in the detection area. Therefore, in theory, when the detection area of the camera and the photodiode is the same, under different light intensities, the ratio of the integration (or average value) of the gray value collected by the camera to the corresponding photodiode signal is always constant. Table 3 shows the average gray value, photodiode signal, and their ratios under different light powers. The relative error between the predicted photodiode

Fig. 4 Length information of photodiode signal acquisition system. **a** Camera and connecting sleeve. **b** Photodiode and connecting sleeve
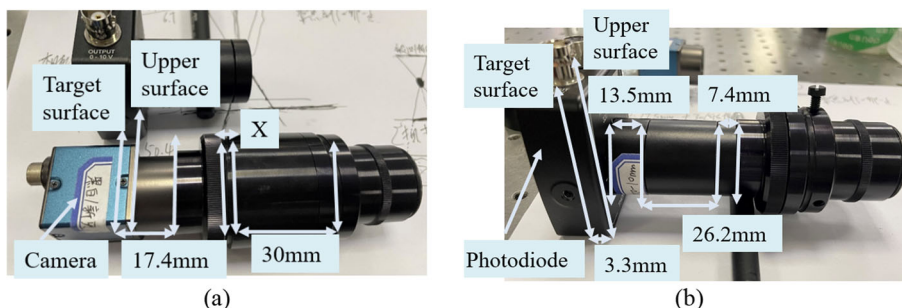
Table 3 Average gray value, photodiode signal, and their ratios under different light powers

Light power (%)	Average gray value	Photodiode signal (V)	Ratios
40	92.6569	0.3841	241.2381
60	126.5560	0.5433	232.9360
80	156.4504	0.6904	226.5936
100	183.1315	0.8267	221.5214
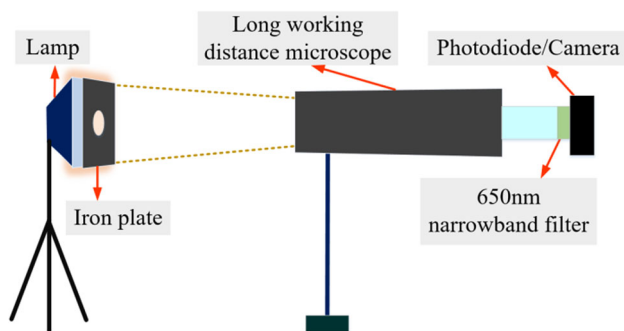
Fig. 5 Schematic diagram of experimental verification of photodiode detection area

signal (0.7840) and the actual photodiode signal (0.8267) is 5.1662% when the average ratio (233.5892) corresponding to 40%, 60%, and 80% of the light power is used to fit the photodiode signal with 100% of the light power. Considering that the field of the camera is not completely identical to that of the hole and that the design optical path itself has errors, the result is acceptable. The experimental verification proves that the detection area of the photodiode can be accurately determined by using the unique photodiode signal acquisition system.

Design of temperature signal acquisition system

The temperature signal acquisition system is mainly based on the principle of dual-wavelength thermometry, and it is designed on the basis of previous work (Feng et al., 2022; Hao et al., 2020).

As shown in Fig. 2, the temperature signal acquisition system mainly includes a dual-channel filter device, a long-focus microscopic lens, and a CMOS camera. The parameters of the long-focus microscopic lens are as follows: the model is LY-WN-SLDM650, the working distance is 13–200 cm, and the maximum spatial resolution is 3 μm. The model of the CMOS camera with 3 million pixels is MER-301-125U3M. The long-focus microscopic lens and camera can enlarge the melt pool temperature field.

The temperature signal acquisition system processes the dual-band melt pool grayscale images into the melt pool temperature field using Eq. (3).

$$T = \frac{\frac{hc}{k}\left(\frac{1}{\lambda_1} - \frac{1}{\lambda_2}\right)}{\ln K + \ln I + 5\ln\frac{\lambda_2}{\lambda_1}} \tag{3}$$

where c represents the speed of light, h represents the Planck constant, k represents the Boltzmann constant, K represents the scale coefficient obtained from the system calibration experiment, and I represents the ratio of the grayscale image obtained under the two bands λ_1 and λ_2.

We take into account the radiation band of the melt pool, plasma interference band, camera sensitivity band, saturation, and temperature measurement range, and set λ_1 and λ_2 to 780 nm and 900 nm, respectively. The bandwidth, transmissivity, and other key parameters of the 780 nm and 900 nm narrowband filters are calculated and designed. In addition, an accurate calibration method for the light splitting proportion distribution of the dual-channel filter device is proposed, a subpixel precision dual-band image matching method is developed, and the method of multi-parameter cooperative optimization and calibration of proportionality coefficients K, λ_1, λ_2 is developed, which provides the measurement system with high-temperature measurement accuracy in harsh conditions such as plasma, soot, and particle splashing. The parameters of the long-focus microscopic lens are as follows: the model is LY-WN-SLDM650, the working distance is 13–200 cm, and the maximum spatial resolution is 3 μm. The model of the CMOS camera with 3 million pixels is MER-301-125U3M. The long-focus microscopic lens and camera can enlarge the melt pool temperature field.

Experiment

In PAW, the forming process of a single line directly determines the quality of the final sample. As the basic unit in the forming process of the sample, the signal change of the melt pool can accurately embody the evolution of the forming process of a single line. The formation and elimination of micro flaws, as well as the regulation of microstructures during AM, are closely related to the spatiotemporal evolution characteristics of the melt pool temperature field. Meanwhile, the abnormal distribution of the melt pool temperature field caused by flaws is a strong signal for the online monitoring of AM. The evolution law of the temperature field in the melt pool shows that the peak temperature of the melt pool causes great interference with flaw detection, and the accuracy of flaw detection near the melt pool can be significantly improved by using the front heating region of the melt pool temperature field (Feng et al., 2022).

Therefore, this research will focus on collecting the radiation light signal from the front heating region of the melt pool temperature field through the optical path design and experimental calibration. This design has three main advantages: 1. The front heating region of the melt pool temperature field is far from the welding gun, and it is less or not affected by the arc light. 2. Once the signal of the front heating region is abnormal, the influence caused by flaws and other factors can be reduced or even eliminated by adjusting the process parameters. 3. The detection area of the photodiode is completely in a melt pool, which effectively avoids the influence of the light outside the melt pool on the photodiode signal and improves the accuracy and sensitivity of the response signal.

Focusing and determination of detection area

As shown in Fig. 2, the photodiode signal acquisition system and temperature signal acquisition system are located on both sides of the PAW working platform. The distance between the long working distance microscope and the substrate is 0.65 m, and the distance between the dual-channel filter device and the substrate is 0.69 m.

After the platform is constructed, it is necessary to perform focusing on the photodiode signal acquisition system and the temperature signal acquisition system, as well as determine the detection areas for both systems. For the temperature signal acquisition system, the developed dual-band image matching method with subpixel accuracy and the proportionality coefficient K, λ_1, λ_2 multi-parameter cooperative optimization and the calibration method (Hao et al., 2020) have completed the focusing. The focusing of the photodiode signal acquisition system is based on the focusing of the temperature signal acquisition system. To ensure that the photodiode can only detect the front heating region of the melt pool temperature field, a ring is added at the front end of the photodiode. The focusing of the photodiode signal acquisition system is completed by replacing the position of the photodiode with a camera and adding a ring at the front end of the camera. After the mark point is made on the substrate, the detection area of the photodiode signal acquisition system is determined by the position of the mark point in the camera field of view. As shown in Fig. 2, the 905 nm narrowband filter is also added to the front end of the photodiode to filter the arc light.

Setting of PAW parameters and experimental design

PAW is affected by many factors, such as ionic gas flow, welding current, welding speed, nozzle distance, and shielding gas flow. These factors usually have a greater impact on the stability of the forming process and the quality of the sample. To avoid a large number of flaws caused by unreasonable parameter settings, the optimal parameters applicable to 314 stainless steel with a diameter of 1.2 mm are selected according to experience. As shown in Table 4, the specific parameter settings are as follows: the peak current is 100 A, the base current is 50 A, the pulse interval is 1 s, the proportions of peak current and base current in a pulse interval are 15% and 85%, respectively, the wire feeding speed is 80 cm/min, the welding speed is 30 mm/min, the plasma gas flow rate is 2 L/min, the shielding gas flow is 15 L/min, and the distance between nozzle and work-piece is 15 mm. The setting of the above experimental parameters is optimal, which has been confirmed in the CT scanning results of the sample because the porosity of the specimen is low. In addition, the frame rate of the temperature signal acquisition system is 125 Hz, and the frame rate of the photodiode signal acquisition system is 250 kHz. As shown in Fig. 6, with a length of approximately 20 mm, two single-line samples are designed. When collecting the photodiode information of single-line 1, a ring with a small radius of 3 mm is added to the front end of the photodiode. When collecting the photodiode information of single-line 2, the front end of the photodiode has no ring (the radius of itself is 4.9 mm), and the starting position of single-line 2 covers the end position of single-line 1. The gray distribution and light intensity signal changes of the arc under the base current are also collected by the platform.

Pretreatment of experimental results

Under the action of peak current, PAW has a large arc energy density and high arc column temperature, which leads to overexposure of the melt pool temperature field calculated by Eq. (3). Therefore, only the melt pool temperature field at the base current is calculated and corrected. Due to the small distance between the welding wire and the melt pool,

Table 4 Specific parameters of PAW

| Peak current (A)	Base current (A)	Pulse interval (s)	Wire feeding speed (cm/min)	Welding Speed (mm/min)	Plasma gas flow rate (L/min)	Shielding gas flow (L/min)	Distance between nozzle and work-piece (mm)
100	50	1	80	30	2	15	15

Fig. 6 Welded sample of single-line 1 (green line) and single-line 2 (black line) (Color figure online)

it is difficult to completely avoid the influence of the welding wire when collecting the melt pool temperature field. Therefore, it is necessary to remove the welding wire from the melt pool temperature field. Besides, the influence of arc light should be eliminated to obtain an effective melt pool temperature field. Figure 7 shows the process of correcting the melt pool temperature field and extracting the local melt pool temperature field. The process of correcting the melt pool temperature field is mainly based on the distribution characteristics of the welding wire and arc light in the grayscale image. Some areas in the effective melt pool temperature field do not have any data. These areas mainly include the area where the welding wire is located and the area where the temperature is far beyond the measurement

range of the temperature signal acquisition system. The blank area where the welding wire is located is represented by a black circle and the letter "W". However, according to the above analysis, the arc light will rotate irregularly due to the influence of the fluid flow. Even after correction, the tail end and central area of the melt pool may also be affected by the arc light at some moments. Therefore, a ring is added to the front of the photodiode to ensure that the detection area is the front heating region of the melt pool temperature field. Through the inverse scale transformation of the aspect ratio of the marking point in the focusing stage of the two systems, the mask of the corresponding region of the ring in the melt pool temperature field can be obtained, and then the high-sensitivity area in the melt pool temperature field and the photodiode detection area are completely coincident. In this way, we simultaneously obtain temperature signals and photodiode signals from the high-sensitivity area of the melt pool, while effectively avoiding the influence of intense arc light and welding wire obstruction.

In addition, since the frame rate of the temperature signal acquisition system is 125 Hz and the frame rate of the photodiode signal acquisition system is 250 kHz, in order to fit the curves of the temperature signal and the photodiode signal, the photodiode signals within each pulse interval are averaged to match the number of temperature signals.

Fig. 7 Process of correcting melt pool temperature field and extracting local areas. W represents the blank area after removing the welding wire inside the black circle
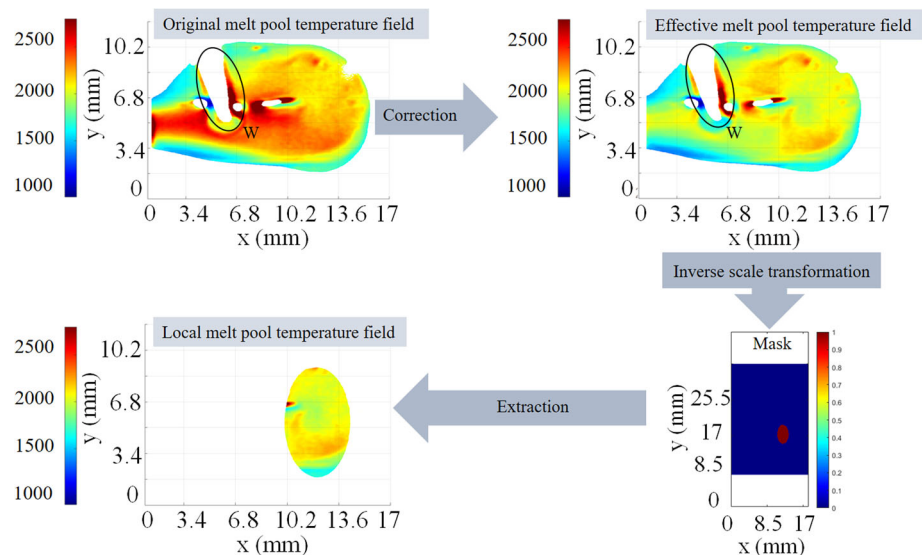
Analysis and discussion of experimental results

The developed platform obtains the evolution process of the melt pool temperature field, estimates the main oscillation frequency, fits the relationship between the photodiode signal and temperature signal, and evaluates the influence of flaws and droplets on the characteristics of the melt pool.

Evolution process of melt pool temperature field

According to the CT scanning results of the two single-line samples shown in Fig. 6, there are no pore flaws in single-line 1, and there are pore flaws in single-line 2. The pore flaws in single-line 2 have no influence on research on the evolution of the melt pool.

In the process of welding single-line 1, the evolution process of the melt pool can be clearly observed in the melt pool temperature field obtained by the temperature signal acquisition system. The timing starts from the end of the preheating phase, and the evolution process is divided into the forming stage, stabilization stage, and cooling stage. This work primarily focuses on the stabilization stage. The stabilization stage lasts for 38 pulse intervals. In this stage, the shape of the melt pool gradually increases from the initial size of 12.8 mm in length and 7.9 mm in width to the final size of 15.1 mm in length and 8.5 mm in width, as shown in Fig. 8. In the 38 pulse intervals, the average temperature of all melt pool temperature fields minimally affected by arc light in each interval is obtained, and the average temperature of the melt pool barely fluctuates.

Estimation of main oscillation frequency

Many researchers (Xiao & Den, 1990, 1993; Aendenroomer & Den, 1998) have studied the correlation between the oscillation frequency and the geometric shape of the melt pool in gas tungsten arc welding (GTAW) technology, which proves the significance of predicting the oscillation frequency of the melt pool. Although PAW is similar to GTAW, there are few studies on estimating the oscillation frequency of the melt pool specifically for PAW technology. Compared with GTAW, PAW has a more concentrated heat source and a greater influence of arc light. Therefore, this work makes full use of the advantages of the developed platform and uses the photodiode signal of the melt pool to study the oscillation frequency. The oscillation index is the photodiode signal of the melt pool obtained by the photodiode signal acquisition system. The photodiode signal represents the sum of the intensity of the radiation light of the melt pool in the detection area, which is consistent with the sum of pixel values in the grayscale image of the melt pool as an indicator in the literature (Caprio et al., 2020). This work mainly estimates

the oscillation frequency of the melt pool when the melt pool characteristics are relatively stable under the base current. Then, the oscillation frequency is evaluated by estimating the PSD. The PSD of the photodiode signal in 38 pulse intervals in the stabilization stage of single-line 1 is calculated with 212,500 data points in each pulse interval. The oscillation frequency of the melt pool is in the low-frequency mode within 200 Hz, and the main oscillation frequency is approximately 20 Hz. The estimation result of the oscillation frequency of the PAW melt pool using the photodiode signal and PSD is consistent with that in the literature (Zhao et al., 2009), which proves the simplicity and effectiveness of the method developed in this work.

The above analysis is not affected by flaws, which can be confirmed by grayscale images of the melt pool and CT scanning results.

Fitting relationship between photodiode signal and temperature signal

In this Section, the fitting relationship between the photodiode signal and the temperature signal of the melt pool under the base current is analyzed n. First, the correlation between the photodiode signal and the temperature signal of the melt pool is analyzed. Then, the real-time representation of the temperature signal using the photodiode signal of the melt pool is explored.

Correlation between photodiode signal and temperature signal

In order to explore the correlation between the photodiode signal and the temperature signal, it is quantitatively represented by the correlation coefficient. The closer the correlation coefficient is to 1, the stronger the positive correlation between the two signals.

According to Eq. (2), the photodiode signal represents the sum of the light intensity in the entire detection area. Theoretically, the correlation between the photodiode signal and the sum of temperature signals in the detection area is expected to be excellent. Considering that the detection area of the photodiode is constant, the correlation between the photodiode signal and the average temperature signal would be appropriate. Moreover, the average temperature is physically more interpretable than the total temperature. In order to demonstrate a better correlation between the photodiode signal and temperature signal within the same area, the correlation coefficients between the local temperature signal and the local photodiode signal are compared with the correlation coefficients between the global temperature signal and the local photodiode signal. In "Pretreatment of experimental results" section, the global temperature field, local temperature field (front heating region), and photodiode signal of

Fig. 8 Evolution process of melt pool in stabilization stage. W represents the blank area after removing the welding wire inside the black circle
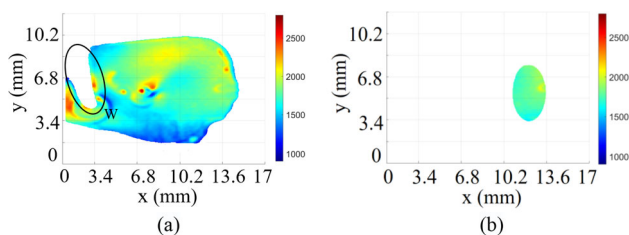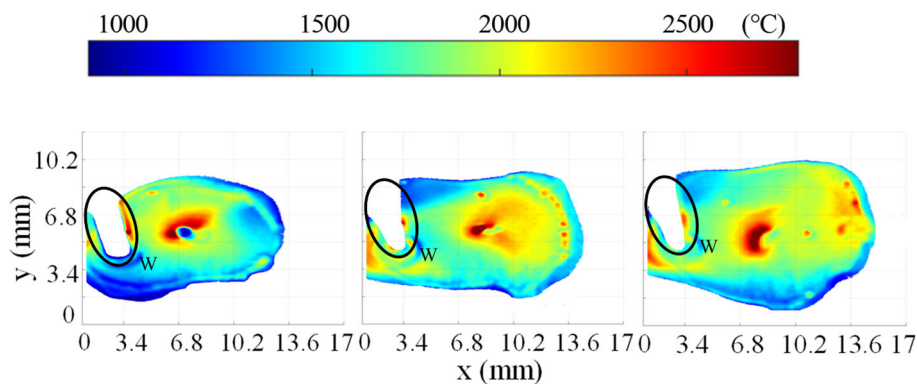
Fig. 9 Melt pool temperature field within 44th pulse interval of single-line 1. **a** Global temperature field. **b** Local temperature field corresponding to detection region of a photodiode with a 3 mm radius circular ring. W represents the blank area after removing the welding wire inside the black circle

the melt pool are obtained and pretreated. In "Evolution process of melt pool temperature field" section, we have already analyzed that the melt pool area is large in the PAW process. Although the radius of the photodiode is 4.9 mm, when there is no 3 mm radius circular ring at the front end of the photodiode, the collected signal still represents a local signal of the melt pool, but with a larger corresponding area of the melt pool.

First, we analyze the correlation between the photodiode signal collected with a ring at the front end and the temperature signal. Figure 9 shows the global temperature field and local temperature field of the melt pool at a certain moment within the 44th pulse interval during the welding process of single-line 1. It should be noted that at this moment, there is a 3 mm radius circular ring at the front end of the photodiode. Figure 10 shows the curves of the photodiode signals, the global average temperature signals, and the local average temperature signals of the melt pool during the 44th pulse interval of single-line 1. Figure 11 shows the fitting line between the photodiode signal and the global average temperature signal, as well as the fitting line between the photodiode signal and the local average temperature signal. The correlation coefficient between the photodiode signals and the local average temperature signals is 0.97, while the correlation coefficient between the photodiode signals and the global average temperature signals is 0.87. Therefore, the
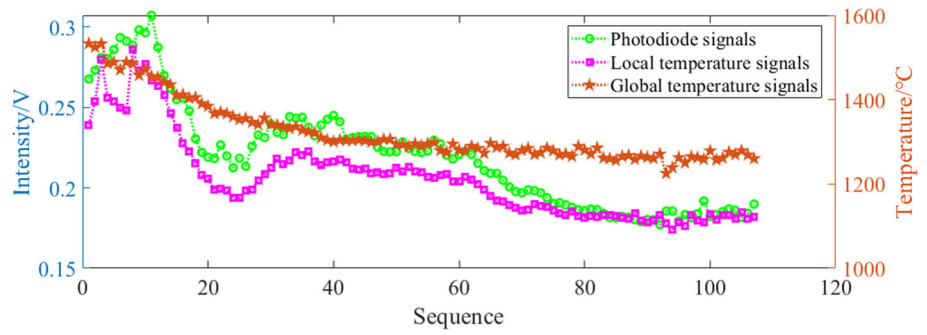
correlation between the photodiode signals and the local average temperature signals of the melt pool is better. The fitting between the photodiode signal and the global average temperature signal is poor, mainly because of the difference in area corresponding to the photodiode signal and the global average temperature signal. The photodiode signals correspond only to the front heating region of the melt pool, while the global average temperature signals correspond to the entire melt pool.

In order to verify whether it is appropriate to correlate the photodiode signal with the local average temperature signal instead of the local total temperature signal, the local total temperature signal of the melt pool is also correlated with the photodiode signal. Figure 12 shows the curves of the photodiode signals and the local total temperature signals of the melt pool during the 44th pulse interval of single-line 1. Figure 13 shows the fitting line between the photodiode signals and the local total temperature signals during the 44th pulse interval of single-line 1. The correlation coefficient between the photodiode signals and the local total temperature signals is 0.92. The correlation coefficients between the photodiode signal and the local average temperature signal, as well as the local total temperature signal, are both above 0.90. Moreover, the correlation coefficient between the photodiode signal and the local average temperature signal is larger. This indicates that it is appropriate to replace the local total temperature signal with the local average temperature signal to correlate with the photodiode signal.

Next, we analyze the correlation between the photodiode signal collected without a ring and the temperature signal. Figure 14 shows the global temperature field and local temperature field of the melt pool at a certain moment within the 48th pulse interval during the welding process of single-line 2.

Figure 15 shows the curves of the photodiode signals, the global average temperature signals, and the local average temperature signals of the melt pool during the 48th pulse interval. Figure 16 shows the fitting line between the photodiode signal and the global average temperature signal, as
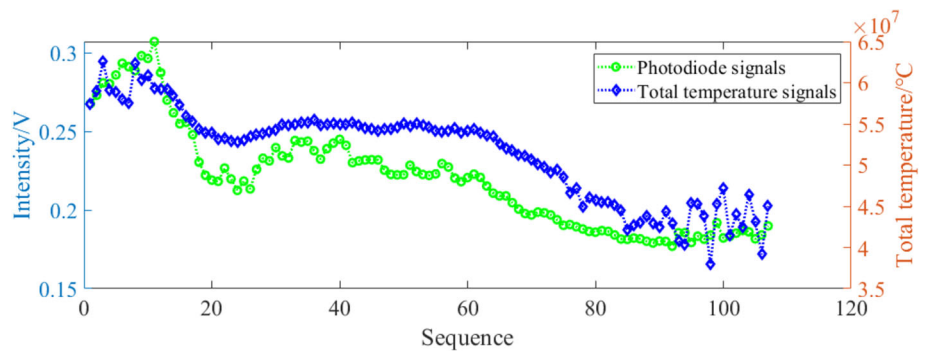
Fig. 10 Curves of photodiode signals, global average temperature signals, and local average temperature signals during the 44th pulse interval of single-line 1. Photodiode signals are collected by the photodiode with a 3 mm radius circular ring
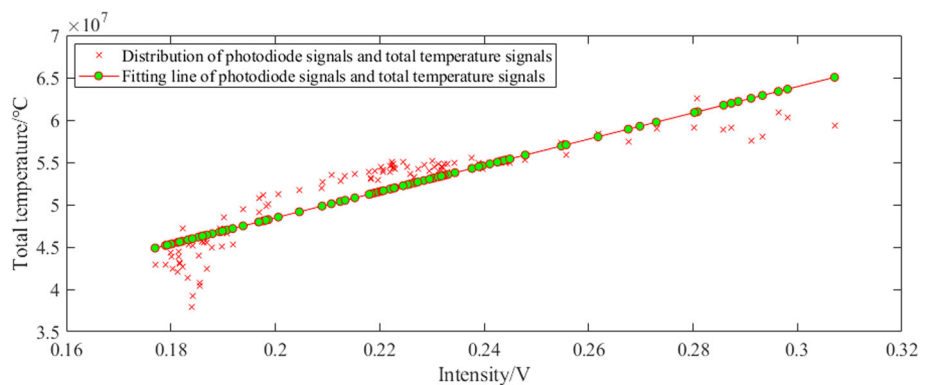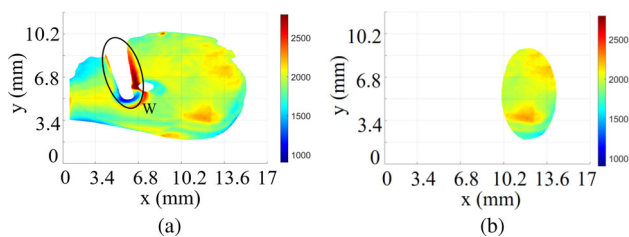

Fig. 11 Fitting lines between photodiode signals and global/local average temperature signals during the 44th pulse interval of single-line 1. Photodiode signals are collected by the photodiode with a 3 mm radius circular ring
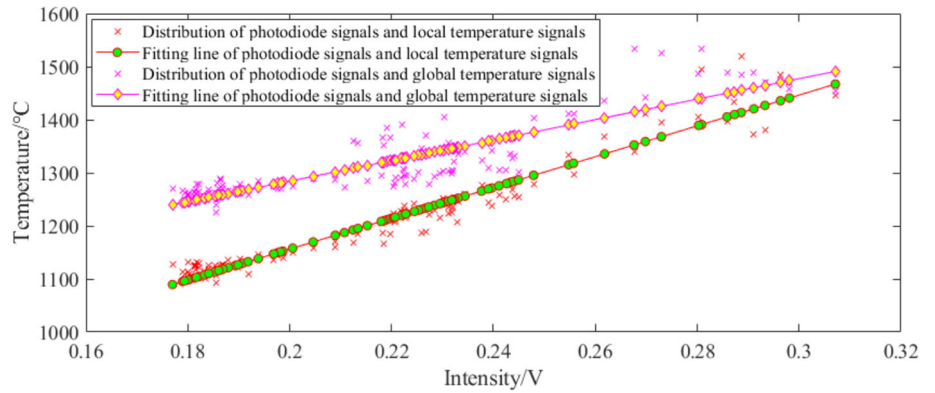
Fig. 12 Curves of photodiode signals and local total temperature signals during the 44th pulse interval of single-line 1. Photodiode signals are collected by a photodiode with a 3 mm radius circular ring

Fig. 13 Fitting lines between photodiode signal and global/local average temperature signals during the 44th pulse interval of single-line 1. Photodiode signals are collected by the photodiode with a 3 mm radius circular ring

Fig. 14 Melt pool temperature field within the 48th pulse interval of single-line 2. **a** Global temperature field. **b** Local temperature field corresponding to detection region of photodiode without a ring. W represents the blank area after removing the welding wire inside the black circle

well as the fitting line between the photodiode signal and the local average temperature signal. The correlation coefficient between the photodiode signals and the local average temperature signals is 0.93, while the correlation coefficient between the photodiode signals and the global average temperature signals is 0.88. Similarly, the correlation between the photodiode signals and the local average temperature signals of the melt pool is better.

Meanwhile, the photodiode signal is also correlated with the local total temperature signal of the melt pool. Figure 17 shows the curves of the photodiode signals and the local total temperature signals of the melt pool during the 48th pulse interval. Figure 18 shows the fitting line between the photodiode signals and the local total temperature signals. The correlation coefficient between the photodiode signal and the local total temperature signal is 0.91, which further

confirms the suitability of correlating the photodiode signal with the local average temperature signal.

Furthermore, through the data analysis of the two single-lines, it is found that the average correlation coefficient between the photodiode signals collected with the ring and the local average temperature signals is slightly higher than the average correlation coefficient between the photodiode signals collected without a ring and the local average temperature signals. The temperature of the melt pool is related to the macrostructure, microstructure, and flaw formation of the sample, and it is a significant melt pool characteristic. The excellent correlation between the photodiode signal and the average temperature signal indicates that the photodiode signal has the potential to represent the average temperature of the melt pool.

Real-time representation of temperature signal

The existing high-speed cameras used for collecting melt pool temperature signals are often limited by transmission rate and memory storage capacity, resulting in their inability to work for extended intervals at high frame rates. Although photodetectors can continuously capture and store data at frame rates of 250 kHz or higher, achieving a complete representation of melt pool characteristics similar to temperature signals using photodiode signals still requires algorithmic processing.
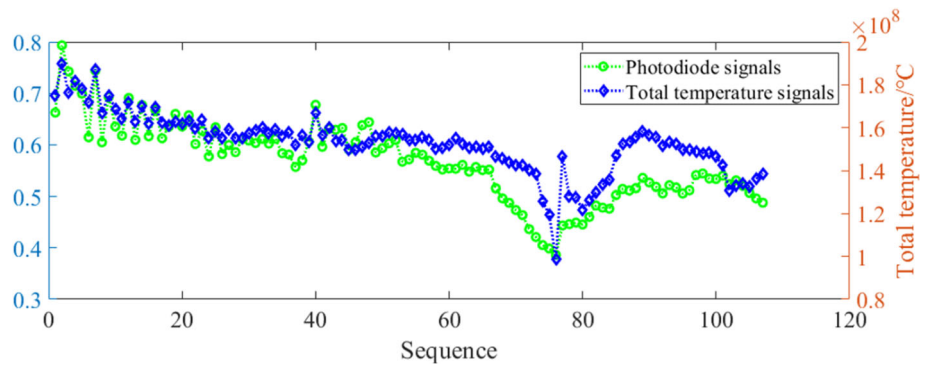
Fig. 15 Curves of photodiode signals, global average temperature signals, and local average temperature signals during the 48th pulse interval of single-line 2. Photodiode signals are collected by the photodiode without a ring
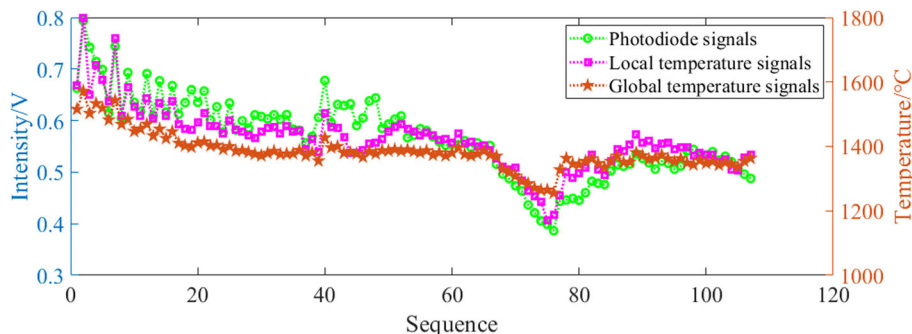

Fig. 16 Fitting lines between photodiode signals and global/local average temperature signals during the 48th pulse interval of single-line 2. Photodiode signals are collected by the photodiode without a ring
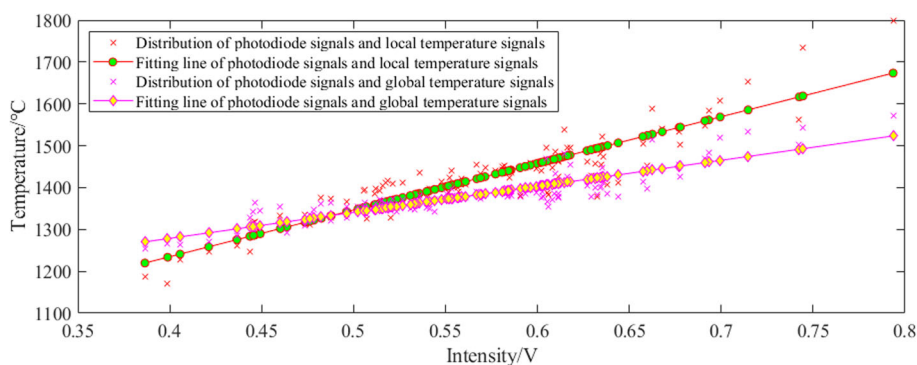
Fig. 17 Curves of photodiode signals and local total temperature signals during the 48th pulse interval of single-line 2. Photodiode signals are collected by the photodiode without a ring

Fig. 18 Fitting lines between photodiode signal and global/local average temperature signals during the 48th pulse interval of single-line 2. Photodiode signals are collected by the photodiode without a ring
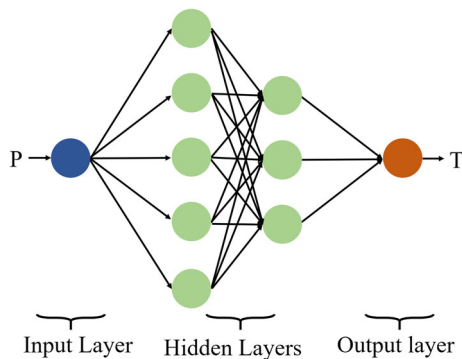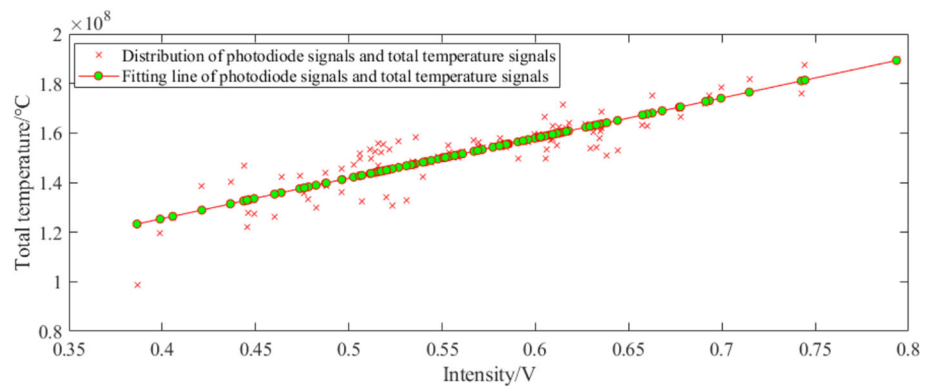
Fig. 19 Schematic diagram of BP neural network

Machine learning is a branch of artificial intelligence that enables computers to learn from data and improve performance automatically using algorithms and statistical models. The backpropagation (BP) neural network is an algorithm in machine learning that is commonly used to predict or estimate object variables. The core idea of the BP neural network is to calculate the error between the predicted values and the actual values, and then propagate the error backwards through the layers to adjust the weights and biases of the network, aiming to minimize the error. As shown in Fig. 19, the BP neural network typically consists of an input layer, hidden layers, and an output layer (Mao et al., 2023). Each node is connected to all nodes in the previous layer and has weights and biases.

Choosing the BP neural network for fitting the photodiode signal and local average temperature signal is based on two reasons. Firstly, correlation between the two signals at the physical level. The photodiode signal corresponds to the radiation light from the melt pool. According to Planck's Radiation Law, radiation light is correlated with temperature. Furthermore, as demonstrated in "Platform design" section, the photodiode signals collected by the platform exhibit a linear relationship with the radiation light. Therefore, the photodiode signal and the temperature signal are correlated on a physical level, as also supported by the signal correlation results presented in "Correlation between photodiode signal and temperature signal" section. Secondly, the applicability of the BP network structure. The BP neural network has the ability to approximate any complex nonlinear function, exhibiting strong fitting capability. Additionally, it demonstrates low latency and fast inference or prediction speed when processing input data, showcasing strong real-time performance. The simplified structure of the BP neural network is suitable for the practical industrial application of the platform because it avoids unnecessary complexity.

The network employs the tansig activation function. The dataset for the BP neural network consists of 9600 pairs of photodiode signals and temperature signals. Among these, 7680 pairs are used as the training set, and 1920 pairs are used as the test set. In Fig. 19, P represents the input photodiode signal, and T represents the output local average temperature

signal. The trained model has an average relative error of 2.82% and is able to output the local average temperature signal in real-time based on the input photodiode signal.

Therefore, when the photodiode signals from the 44th pulse interval of single-line 1 are input into the model, the predicted local temperature signals are obtained. Figure 20 shows the curves of the photodiode signals, the predicted local temperature signals, and the ground-truth local temperature signals. The correlation coefficient between the photodiode signals and the predicted local temperature signals is 0.96, which is the same as the correlation coefficient of 0.96 between the photodiode signals and the ground-truth local temperature signals. The correlation coefficient between the predicted local temperature signals and the ground-truth local temperature signals is 0.97, which is higher than the correlation coefficient between the photodiode signals and the ground-truth local temperature signals. Additionally, as the variation coefficient can further reflect the relative fluctuation of the curves (Mao et al., 2023; Zhang et al., 2021), the variation coefficients of the photodiode signals, predicted local temperature signals, and ground-truth local temperature signals are compared. The values of the variable coefficient of the photodiode signals, predicted local temperature signals, and ground-truth local temperature signals are 0.151, 0.088, and 0.082, respectively. Therefore, the comparative results of correlation coefficients and variation coefficients have demonstrated that the predicted local temperature signal is closer to the ground-truth local temperature signals compared to the photodiode signal. Consequently, the representation capability of the photodiode signal for melt pool characteristics has been optimized through training.

Figure 21 shows the relative error distribution between the predicted local temperature signals and the ground-truth local temperature signals. The average relative error of predicted temperature signals and ground-truth temperature signals is 1.52%, demonstrating that the model can output high-precision temperature signals in real-time.

Melt pool characteristics under influences of droplets and flaws

In this Section, the influence of flaws and droplets on the characteristics of the melt pool is analyzed. First, the abnormal variations in melt pool characteristics caused by droplets are estimated by combining the grayscale image of the melt pool and the photodiode signals. Then the abnormal variations in melt pool characteristics caused by flaws are estimated and verified by combining the rich information from the melt pool temperature field and the scanning results from CT.

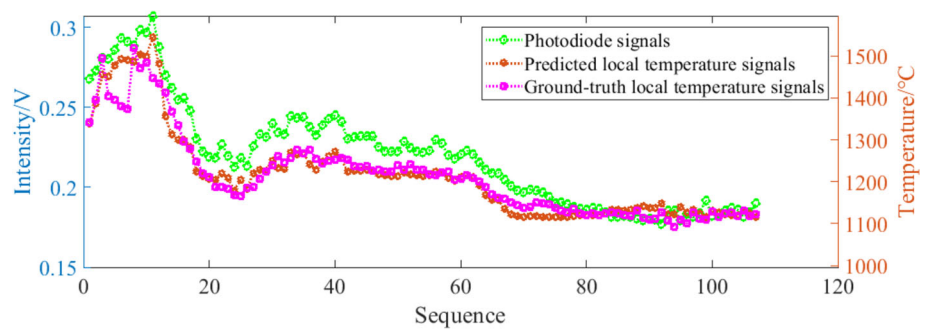## Melt pool characteristics under influences of droplets

As shown by the blue circle in Fig. 22, there is significant fluctuation in the photodiode signals and temperature signals during the initial stage of the 27th pulse interval in single-line 1 under the influence of the base current. This is believed to be attributed to the frequent droplet transfer. Figure 22 shows the curves of the photodiode signals, the predicted local temperature signals, and the ground-truth local temperature signals of the melt pool during the pulse interval. The correlation coefficient between the photodiode signals and the actual ground-truth local temperature signals is 0.97, while the correlation coefficient between the photodiode signals and the predicted local temperature signals is 0.98. The correlation coefficient between the predicted local temperature signals and the ground-truth local temperature signals is 0.98, which is higher than the correlation coefficient between the photodiode signals and the ground-truth local temperature signals. The values of the variable coefficient of the photodiode signals, predicted local temperature signals, and ground-truth local temperature signals are 0.136, 0.185, and 0.182, respectively. Therefore, the comparative results of correlation coefficients and variation coefficients have demonstrated that the predicted local temperature signal is closer to the ground-truth local temperature signals compared to the photodiode signal under influences of droplets.

Figure 23 shows the relative error distribution between the predicted local temperature signals and the ground-truth local temperature signals. Simultaneously, the average relative error of predicted temperature signals and ground-truth temperature signals is 2.23%.

Before droplets melt into the melt pool, they are not part of the melt pool. Therefore, the droplet transfer process cannot be directly observed through the melt pool temperature field. As shown in Fig. 24, continuous grayscale images of the melt pool are used to observe droplets. The droplets in the blue circle have just formed, and the droplets in the green circle are melting into the melt pool. The dropping frequency of the droplet is consistent with the fluctuation frequency of the temperature signals and photodiode signals shown in Fig. 22. The droplet transfer increases the energy of the melt pool, while the heat exchange between the melt pool and the environment leads to energy dissipation. The droplet transfer that occurs at the initial stage of the base current causes obvious fluctuations in the temperature signals and photodiode signals, and the main oscillation frequency is approximately 64 Hz.

Therefore, in the presence of droplet influence causing significant signal fluctuations, the fitting relationship between the temperature signal and the photodiode signal is still excellent, and the model remains robust.
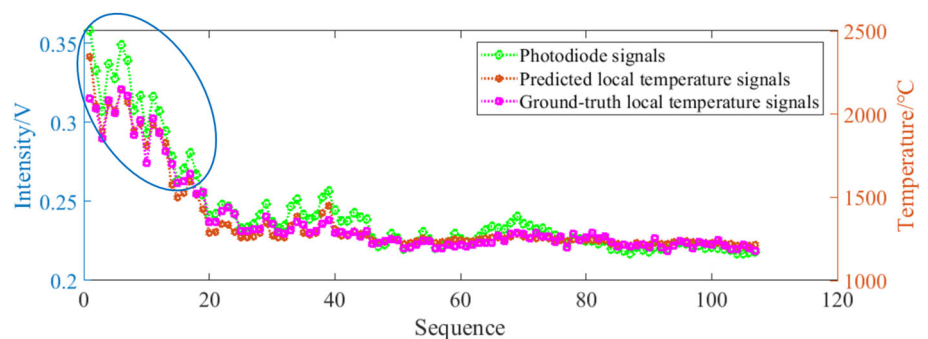
Fig. 20 Curves of photodiode signals, predicted local temperature signals, and ground-truth local temperature signals during the 44th pulse interval of single-line 1. Photodiode signals are collected by the photodiode with a 3 mm radius circular ring

Fig. 21 Relative error distribution between predicted local temperature signals and ground-truth local temperature signals during the 44th pulse interval of single-line 1
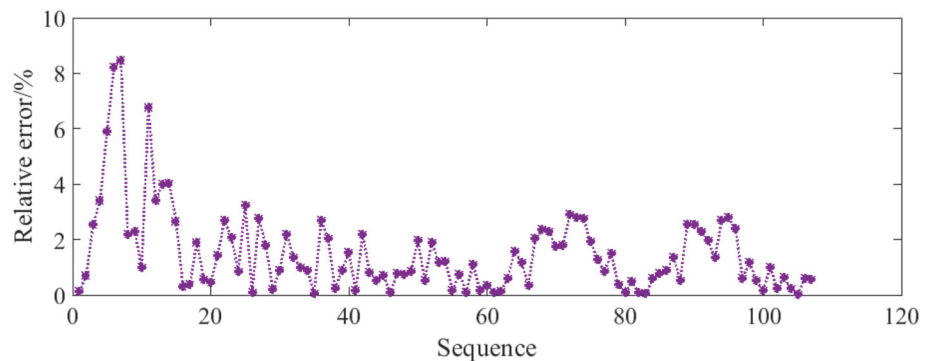
Fig. 22 Curves of photodiode signals, predicted local temperature signals, and ground-truth local temperature signals during 27th pulse interval of single-line 1. Photodiode signals are collected by a photodiode with a 3 mm radius circular ring. The blue circle represents abnormal variations in signals (Color figure online)

Melt pool characteristics under influences of flaws

As shown by the blue circles in Fig. 25, there are abnormal variations in the photodiode signals and temperature signals during the 40th pulse interval and the 33rd pulse interval in single-line 2 under the influence of the base current. The abnormal variations are primarily characterized by an average difference in amplitude between adjacent signals that is 8–12 times higher than in other time intervals.

Figure 25 shows the curves of the photodiode signals, the predicted local temperature signals, and the ground-truth local temperature signals of the melt pool during the 40th and the 33rd pulse interval.

During the 40th pulse interval, the correlation coefficient between the photodiode signals and the ground-truth local temperature signals is 0.91, while the correlation coefficient between the photodiode signals and the predicted local temperature signals is 0.90. The correlation coefficient between the predicted local temperature signals and the ground-truth local temperature signals is 0.93, which is higher than the correlation coefficient between the photodiode signals and the ground-truth local temperature signals. The values of the variable coefficient of the photodiode signals, predicted local temperature signals, and ground-truth local temperature signals are 0.155, 0.076, and 0.084, respectively.

During the 33rd pulse interval, the correlation coefficient between the photodiode signals and the ground-truth local temperature signals is 0.94, while the correlation coefficient between the photodiode signals and the predicted local temperature signals is 0.95. The correlation coefficient between the predicted local temperature signals and the ground-truth local temperature signals is 0.96, which is higher than the correlation coefficient between the photodiode signals and the ground-truth local temperature signals. The values of the variable coefficient of the photodiode signals, predicted local
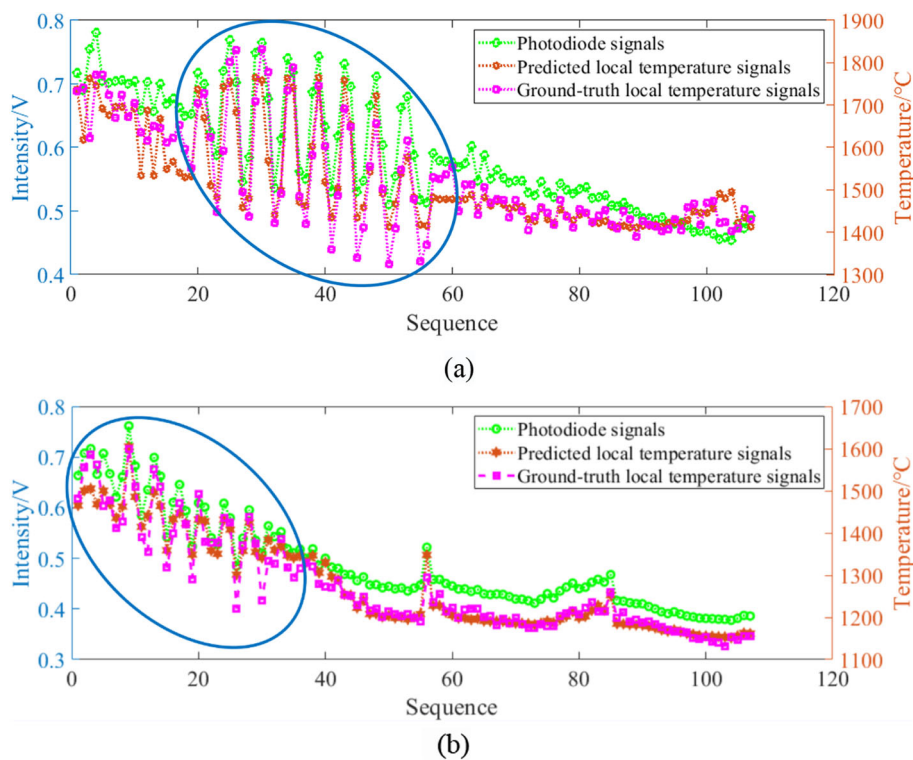
Fig. 23 Relative error distribution between predicted local temperature signals and ground-truth local temperature signals during the 27th pulse interval of single-line 1
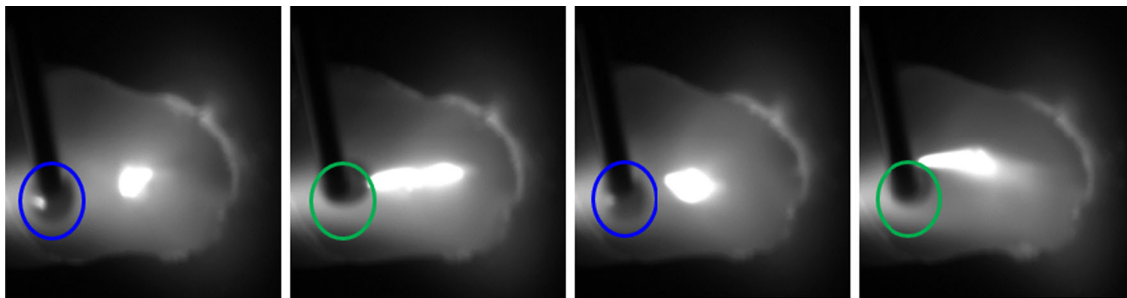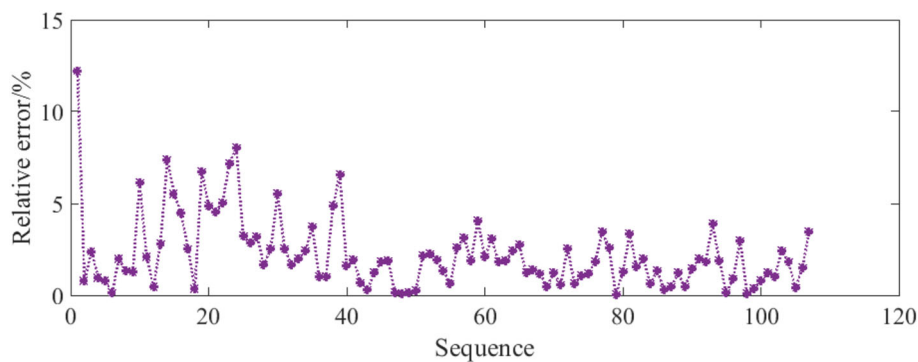

Fig. 24 Droplet transfer process observed from grayscale images of the melt pool. The blue circles represent newly formed droplets, while the green circles represent droplets that are melting into the melt pool (Color figure online)

Fig. 25 Curves of photodiode signals, predicted local temperature signals, and ground-truth local temperature signals. **a** During the 40th pulse interval of single-line 2. **b** During the 33rd pulse interval of single-line 2. Photodiode signals are collected by a photodiode without a ring. The red circle represents the anomalous high-temperature point. The blue circle represents abnormal variations in signals (Color figure online)

(a)

(b)

Fig. 26 Relative error distribution between predicted local temperature signals and ground-truth local temperature signals. **a** During the 40th pulse interval of single-line 2. **b** During the 33rd pulse interval of single-line 2

(a)

(b)
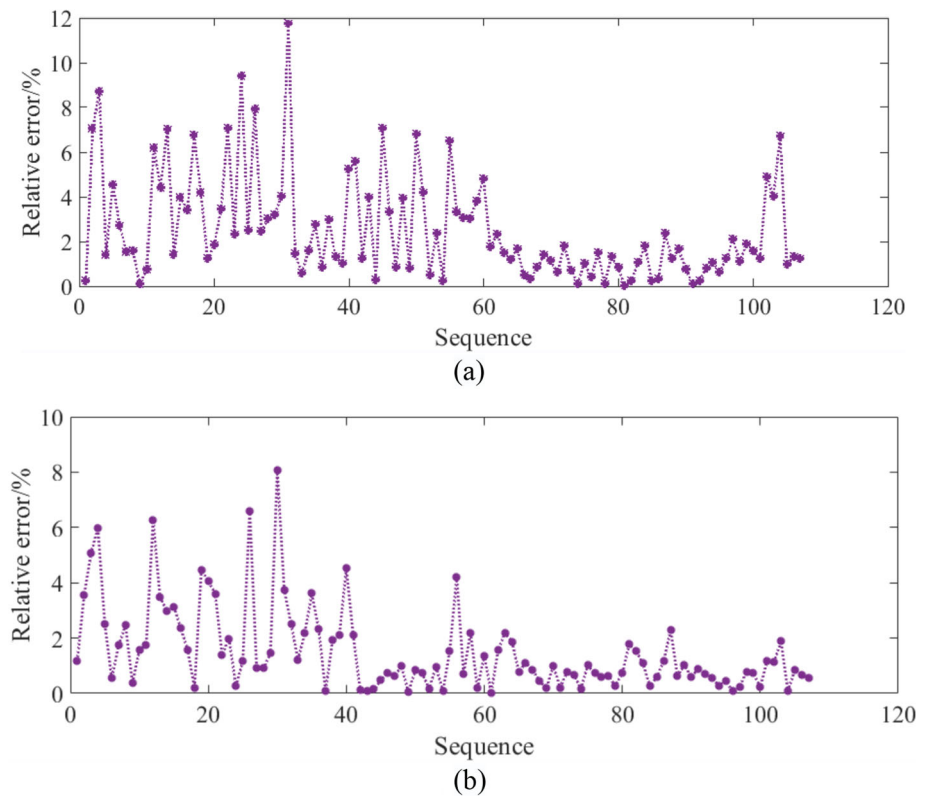
temperature signals, and ground-truth local temperature signals are 0.193, 0.090, and 0.091, respectively.

Therefore, the comparative results of correlation coefficients and variation coefficients have demonstrated that the predicted local temperature signal is closer to the ground-truth local temperature signals compared to the photodiode signal under influences of flaws.

Figure 26 shows the relative error distribution between the predicted local temperature signals and the ground-truth local temperature signals of the melt pool during the 40th and the 33rd pulse intervals. The average relative error of predicted temperature signals and ground-truth temperature signals during the 40th pulse interval is 2.47%, while during the 33rd pulse interval, it is 2.35%.

Therefore, even in the presence of abnormal variations, the fitting relationship between the temperature signal and the photodiode signal is still excellent, and the model remains robust.

To identify the cause of the abnormal variations during the 40th and 33rd pulse interval of single-line 2, we obtained the global temperature field and local temperature field of the melt pool corresponding to the time of the anomalies. Representative images of the global temperature field and local temperature field are shown in Fig. 27. During the two-time intervals when the abnormal variations occurred, the melt pool front encounters the spatter, and there is an anomalous high-temperature point between them, as indicated by the

red circle in Fig. 27. The previous work (Khairallah et al., 2020) has demonstrated that spatter is an influencing factor in the occurrence of flaws during the AM process. Therefore, the heat transfer between the spatter and the melt pool may lead to abnormal variations in local temperature. Under the influence of buoyancy, Lorentz force, surface tension, arc pressure, self-gravity, and droplet transfer, the flow behaviors of the melt pool are complex rotational flow motions. In this scenario, the main oscillation frequency of the melt pool increases to 32–36 Hz, which is higher than the main oscillation frequency under normal conditions. The possible reason is that when the melt pool encounters the spatter, the spatter resists the flow of the melt pool, making the flow behaviors of the melt pool more complex. In particular, the rebound of flow velocity can result in short-term disturbances on the melt pool surface, and these disturbances may lead to an increase in the main oscillation frequency.

To further confirm that the abnormal variations reflect the process of flaw formation, the CT scanning results of single-line 2 are analyzed. According to the CT scanning results shown in Fig. 28, it can be observed that pore flaws with diameters of 0.13 mm (in the red circle) and 0.15 mm (in the black circle) are generated during the welding process of single-line 2. Based on the three-dimensional coordinates of the pore flaws and the welding speed, it can be determined that the time of pore flaw occurrence corresponds to the abnormal intervals in the 40th and 33rd pulse intervals.
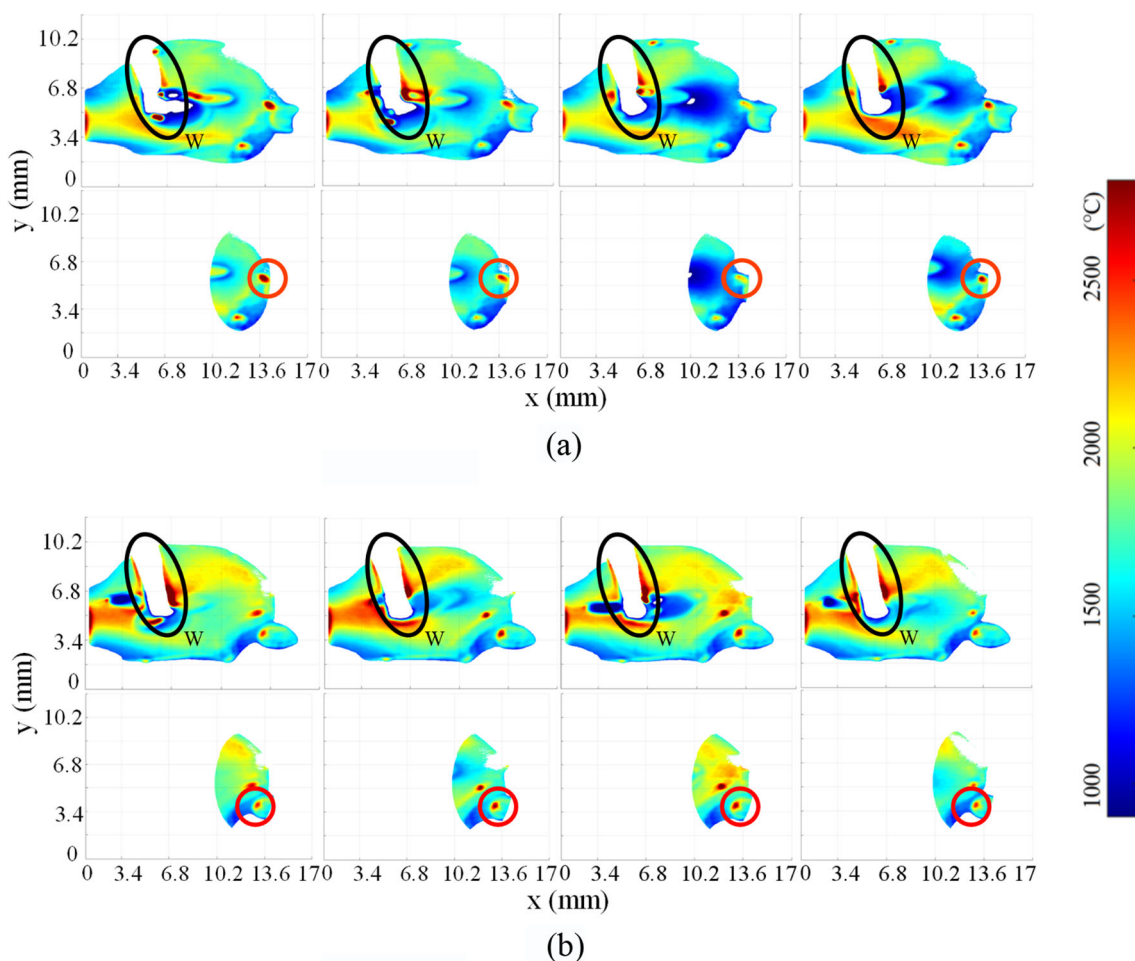
Fig. 27 Global temperature field (upper) and local temperature field (lower) of melt pool. **a** During the 40th pulse interval of single-line 2. **b** During the 33rd pulse interval of single-line 2. W represents the blank area after removing the welding wire inside the black circle. The red circle represents the anomalous high-temperature point (Color figure online)

Therefore, the developed platform can convert photodiode signals into real-time temperature signals in a long-term manner through the model, and then accurately detect the generation of flaws based on the specific threshold of the amplitude difference between adjacent signals. However, it must be noted that the current platform is primarily suitable for detecting anomalies caused by significant defects such as spatter, and the detection indices also have limitations and practical considerations. For smaller defects or processes with very small melt pools, it is necessary to fully utilize other information from the melt pool signal, such as frequency (Ren et al., 2023).

Conclusion

In this work, the melt pool characteristics detection platform based on multi-information fusion is developed. The platform primarily consists of a unique photodiode signal acquisition system and a designed temperature signal acquisition system.

Firstly, the unique photodiode signal acquisition system accurately collects the photodiode signals from the high-sensitivity area of the melt pool by enlarging the field of view and optimizing the detection area. Secondly, the temperature signal acquisition system obtains the global temperature field and the local temperature field of the melt pool. Thirdly, the platform continuously and in real-time obtains high-precision temperature signals from the melt pool. Finally, the platform detects the generation of flaws based on real-time abnormal variations in temperature signals. Therefore,
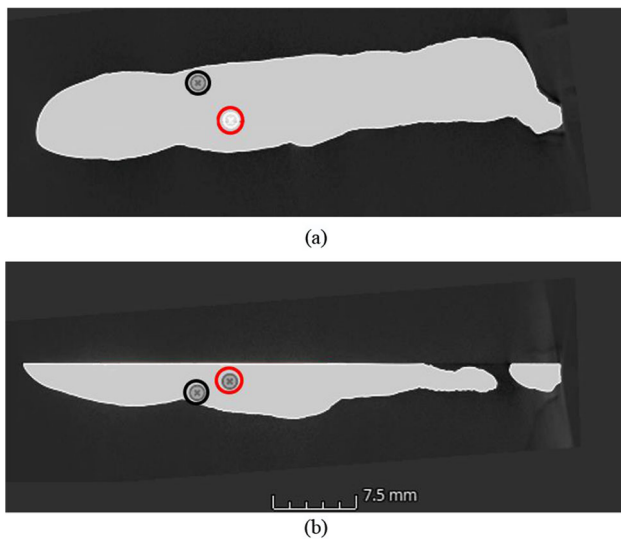
Fig. 28 Views of CT scanning results. **a** Top view. **c** Side view. The red circle and black circle represent the pore flaw (Color figure online)

this platform can provide important technical and data support for sample quality evaluation and intelligent control of the PAW process.

The main focus of future research is to utilize two photodiodes and the colorimetric temperature measurement principle to detect the melt pool temperature. This approach avoids the dependency on the object's emissivity and overcomes the influence of measurement environment, distance, angle, and other factors. Additionally, the melt pool temperature field acquisition system can be eliminated, significantly reducing the economic cost and better meeting the practical needs of the industry.

Data availability The data that support the findings of this study are available from the corresponding author upon request.

Declarations

Competing interests The authors declare that they have no known competing financial interests or personal relationships that could have appeared to influence the work reported in this paper.

References

Aendenroomer, A. J. R., & Den, O. G. (1998). Weld pool oscillation as a tool for penetration sensing during pulsed GTA welding. *Welding Journal, 77*, 181-s.

Berumen, S., Bechmann, F., Lindner, S., et al. (2010). Quality control of laser-and powder bed-based Additive Manufacturing (AM) technologies. *Physics Procedia, 5*, 617–622. https://doi.org/10.1016/j.phpro.2010.08.089

Boone, N., Zhu, C., Smith, C., et al. (2018). Thermal near infrared monitoring system for electron beam melting with emissivity tracking. *Additive Manufacturing, 22*, 601–605. https://doi.org/10.1016/j.addma.2018.06.004

Caprio, L., Demir, A. G., & Previtali, B. (2020). Observing molten pool surface oscillations during keyhole processing in laser powder bed fusion as a novel method to estimate the penetration depth. *Additive Manufacturing, 36*, 101470. https://doi.org/10.1016/j.addma.2020.101470

Clijsters, S., Craeghs, T., Buls, S., et al. (2014). In situ quality control of the selective laser melting process using a high-speed, real-time melt pool monitoring system. *The International Journal of Advanced Manufacturing Technology, 75*(5), 1089–1101. https://doi.org/10.1016/S0924-0136(01)00522-2

de Winton, H. C., Cegla, F., & Hooper, P. A., et al. (2021). A method for objectively evaluating the defect detection performance of in-situ monitoring systems. *Additive Manufacturing, 48*, 102431. https://doi.org/10.1016/j.addma.2021.102431

Dunbar, A. J., & Nassar, A. R. (2018). Assessment of optical emission analysis for in-process monitoring of powder bed fusion additive manufacturing. *Virtual and Physical Prototyping, 13*(1), 14–19. https://doi.org/10.1080/17452759.2017.1392683

Everton, S. K., Hirsch, M., Stravroulakis, P., et al. (2016). Review of in-situ process monitoring and in-situ metrology for metal additive manufacturing. *Materials & Design, 95*, 431–445. https://doi.org/10.1016/j.matdes.2016.01.099

Feng, W., Mao, Z., Yang, Y., et al. (2022). Online defect detection method and system based on similarity of the temperature field in the melt pool. *Additive Manufacturing, 54*, 102760. https://doi.org/10.1016/j.addma.2022.102760

Gökhan, D. A., De Giorgi, C., & Previtali, B. (2018). Design and implementation of a multisensor coaxial monitoring system with correction strategies for selective laser melting of a maraging steel. *Journal of Manufacturing Science and Engineering, 140*(4), 041003. https://doi.org/10.1115/1.4038568

Hao, C., Liu, Z., Xie, H., et al. (2020). Real-time measurement method of melt pool temperature in the directed energy deposition process. *Applied Thermal Engineering, 177*, 115475. https://doi.org/10.1016/j.applthermaleng.2020.115475

Hojjatzadeh, S. M. H., Parab, N. D., Yan, W., et al. (2019). Pore elimination mechanisms during 3D printing of metals. *Nature Communications, 10*(1), 3088. https://doi.org/10.1038/s41467-019-10973-9

Jayasinghe, S., Paoletti, P., Sutcliffe, C., et al. (2022). Automatic quality assessments of laser powder bed fusion builds from photodiode sensor measurements. *Progress in Additive Manufacturing*. https://doi.org/10.1007/s40964-021-00219-w

Khairallah, S. A., Martin, A. A., Lee, J. R. I., et al. (2020). Controlling interdependent meso-nanosecond dynamics and defect generation in metal 3D printing. *Science, 368*(6491), 660–665. https://doi.org/10.1126/science.aay7830

Khanzadeh, M., Chowdhury, S., Tschopp, M. A., et al. (2019). In-situ monitoring of melt pool images for porosity prediction in directed energy deposition processes. *IISE Transactions, 51*(5), 437–455. https://doi.org/10.1080/24725854.2017.1417656

Kirka M. M., Fernandez-Zelaia P., Lee Y., et al. (2020). Mechanical performance of a non-weldable ni-base superalloy: Inconel 738 fabricated by electron beam melting. In: *Superalloys 2020: Proceedings of the 14th international symposium on superalloys*. Springer. https://doi.org/10.1007/978-3-030-51834-9_105

Kriczky, D. A., Irwin, J., Reutzel, E. W., et al. (2015). 3D spatial reconstruction of thermal characteristics in directed energy deposition through optical thermal imaging. *Journal of Materials Processing Technology, 221*, 172–186. https://doi.org/10.1016/j.jmatprotec.2015.02.021

Kruth, J. P., Duflou, J., Mercelis, P., et al. (2007). On-line monitoring and process control in selective laser melting and laser cutting//Proceedings of the 5th Lane Conference. *Laser Assisted Net Shape Engineering, 1*, 23–37.

Lapointe, S., Guss, G., Reese, Z., et al. (2022). Photodiode-based machine learning for optimization of laser powder bed fusion parameters in complex geometries. *Additive Manufacturing, 53*, 102687. https://doi.org/10.1016/j.addma.2022.102687

Liu, W. W., Tang, Z. J., Liu, X. Y., et al. (2017a). A review on in-situ monitoring and adaptive control technology for laser cladding remanufacturing. *Procedia Cirp, 61*, 235–240. https://doi.org/10.1016/j.procir.2016.11.217

Liu, X. F., Jia, C. B., Wu, C. S., et al. (2017b). Measurement of the keyhole entrance and topside weld pool geometries in keyhole plasma arc welding with dual CCD cameras. *Journal of Materials Processing Technology, 248*, 39–48. https://doi.org/10.1016/j.jmatprotec.2017.05.012

Liu, X. F., Wu, C. S., Jia, C. B., et al. (2017c). Visual sensing of the weld pool geometry from the topside view in keyhole plasma arc welding. *Journal of Manufacturing Processes, 26*, 74–83. https://doi.org/10.1016/j.jmapro.2017.01.011

Liu, Z., Wu, C., Cui, S., et al. (2017d). Correlation of keyhole exit deviation distance and weld pool thermo-state in plasma arc welding process. *International Journal of Heat and Mass Transfer, 104*, 310–317. https://doi.org/10.1016/j.ijheatmasstransfer.2016.08.069

Liu, Z., Wu, C. S., & Gao, J. (2013). Vision-based observation of keyhole geometry in plasma arc welding. *International Journal of Thermal Sciences, 63*, 38–45. https://doi.org/10.1016/j.ijthermalsci.2012.07.006

Ma, H., Mao, Z., Feng, W., et al. (2022). Online in-situ monitoring of melt pool characteristic based on a single high-speed camera in laser powder bed fusion process. *Applied Thermal Engineering, 211*, 118515. https://doi.org/10.1016/j.applthermaleng.2022.118515

Mao, Z., Feng, W., Ma, H., et al. (2023). Continuous online flaws detection with photodiode signal and melt pool temperature based on deep learning in laser powder bed fusion. *Optics & Laser Technology, 158*, 108877. https://doi.org/10.1016/j.optlastec.2022.108877

Ren, Z., Gao, L., Clark, S. J., et al. (2023). Machine learning–aided real-time detection of keyhole pore generation in laser powder bed fusion. *Science, 379*(6627), 89–94. https://doi.org/10.1126/science.add4667

Rezaeifar, H., & Elbestawi, M. A. (2021). On-line melt pool temperature control in L-PBF additive manufacturing. *The International Journal of Advanced Manufacturing Technology, 112*, 2789–2804. https://doi.org/10.1007/s00170-020-06441-0

Saad, E., Wang, H., & Kovacevic, R. (2006). Classification of molten pool modes in variable polarity plasma arc welding based on acoustic signature. *Journal of Materials Processing Technology, 174*(1–3), 127–136. https://doi.org/10.1016/j.jmatprotec.2005.03.020

Spears, T. G., & Gold, S. A. (2016). In-process sensing in selective laser melting (SLM) additive manufacturing. *Integrating Materials and Manufacturing Innovation, 5*(1), 16–40. https://doi.org/10.1186/s40192-016-0045-4

Sun, Y., Gu, D., Dai, D., et al. (2020). Thermal behavior and microstructure evolution mechanism of W-20% Fe alloy fabricated by laser metal deposition. *International Journal of Mechanical Sciences, 183*, 105772. https://doi.org/10.1016/j.ijmecsci.2020.105772

Taherkhani, K., Sheydaeian, E., Eischer, C., et al. (2021). Development of a defect-detection platform using photodiode signals collected from the melt pool of laser powder-bed fusion. *Additive Manufacturing, 46*, 102152. https://doi.org/10.1016/j.addma.2021.102152

Veiga, F., Suarez, A., Aldalur, E., et al. (2022). Wire arc additive manufacturing of invar parts: Bead geometry and melt pool monitoring. *Measurement, 189*, 110452. https://doi.org/10.1016/j.measurement.2021.110452

Wang, H., & Kovacevic, R. (2002). On-line monitoring of the keyhole welding pool in variable polarity plasma arc welding. *Proceedings of the Institution of Mechanical Engineers, Part B: Journal of Engineering Manufacture, 216*(9), 1265–1276. https://doi.org/10.1243/095440502760291817

Wang, Y., & Chen, Q. (2002). On-line quality monitoring in plasma-arc welding. *Journal of Materials Processing Technology, 120*(1–3), 270–274. https://doi.org/10.1016/S0924-0136(01)01190-6

Wu, B., Pan, Z., Ding, D., et al. (2018). A review of the wire arc additive manufacturing of metals: Properties, defects and quality improvement. *Journal of Manufacturing Processes, 35*, 127–139. https://doi.org/10.1016/j.jmapro.2018.08.001

Wu, D., Hu, M., Huang, Y., et al. (2021). In situ monitoring and penetration prediction of plasma arc welding based on welder intelligence-enhanced deep random forest fusion. *Journal of Manufacturing Processes, 66*, 153–165. https://doi.org/10.1016/j.jmapro.2021.04.007

Wu, D., Huang, Y., Zhang, P., et al. (2020). Visual-acoustic penetration recognition in variable polarity plasma arc welding process using hybrid deep learning approach. *IEEE Access, 8*, 120417–120428. https://doi.org/10.1109/ACCESS.2020.3005822

Xia, C., Pan, Z., Li, Y., et al. (2022). Vision-based melt pool monitoring for wire-arc additive manufacturing using deep learning method. *The International Journal of Advanced Manufacturing Technology, 120*(1–2), 551–562. https://doi.org/10.1007/s00170-022-08811-2

Xiao, Y. H., & Den, O. G. (1990). A study of GTA weld pool oscillation. *Welding Journal, 69*(8), 289.

Xiao, Y. H., & Den, O. G. (1993). Weld pool oscillation during GTA welding of mild steel. *Welding Journal-New York-, 72*, 428-s.

Zhang, G., Wu, C. S., & Liu, Z. (2014). Experimental observation of both keyhole and its surrounding thermal field in plasma arc welding. *International Journal of Heat and Mass Transfer, 70*, 439–448. https://doi.org/10.1016/j.ijheatmasstransfer.2013.11.036

Zhang, P., Zhou, X., Ma, H., et al. (2021). Anomaly detection in laser metal deposition with photodiode-based melt pool monitoring system. *Optics & Laser Technology, 144*, 107454. https://doi.org/10.1016/j.optlastec.2021.107454

Zhang, Y., Mi, J., Li, H., et al. (2022). In situ monitoring plasma arc additive manufacturing process with a fully convolutional network. *The International Journal of Advanced Manufacturing Technology, 120*(3–4), 2247–2257. https://doi.org/10.1007/s00170-022-08929-3

Zhao, C. X., Van Steijn, V., Richardson, I. M., et al. (2009). Experimental characterization of GTA weld pool surface flow using PIV. In: *Trends in welding research 2008: proc. 8th int. conf* (pp. 201–210).